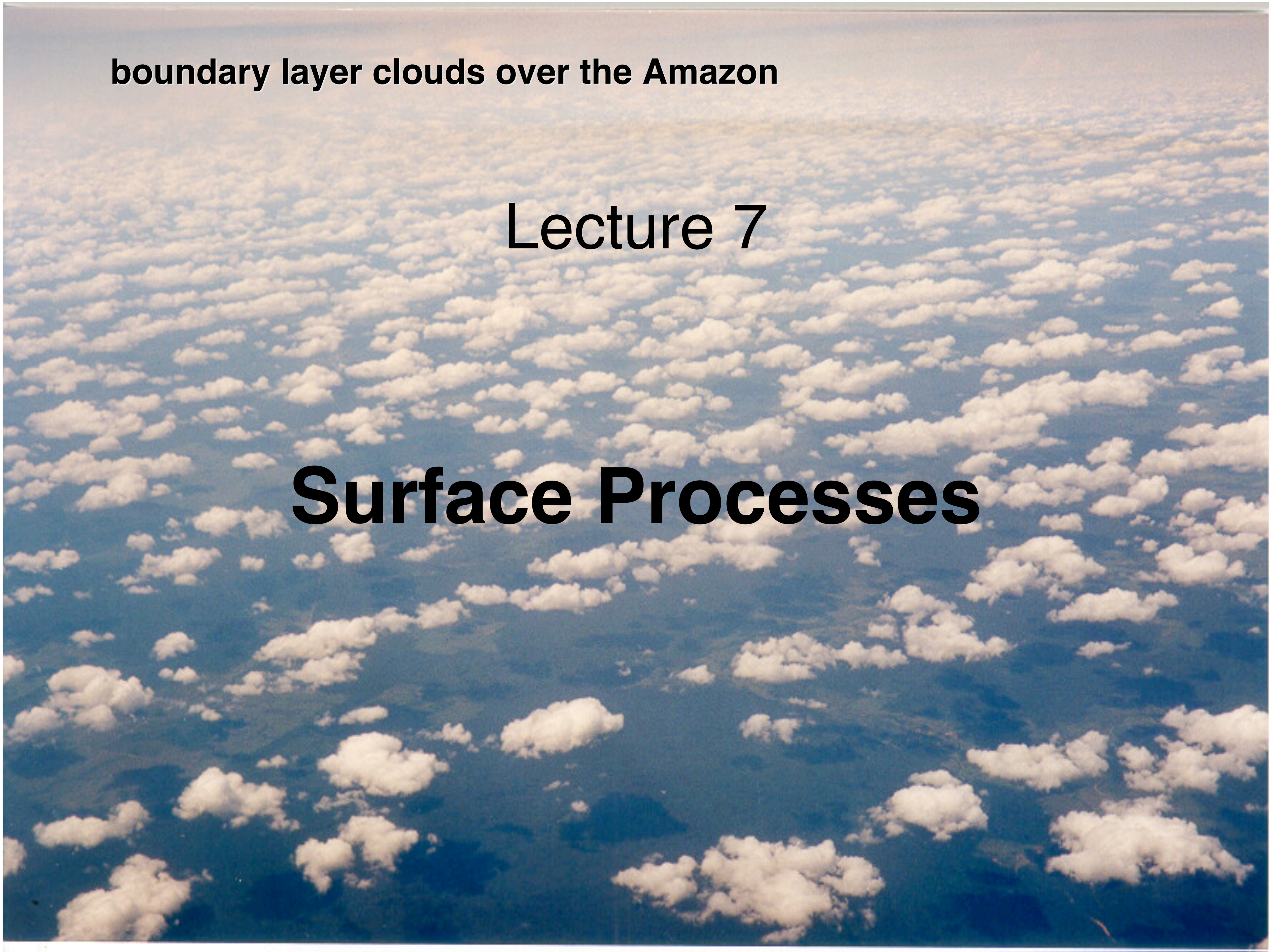
boundary layer clouds over the Amazon
Lecture 7
Surface Processes

SURFACE HEAT BUDGET: BACKGROUND

Surface Energy Budget Components

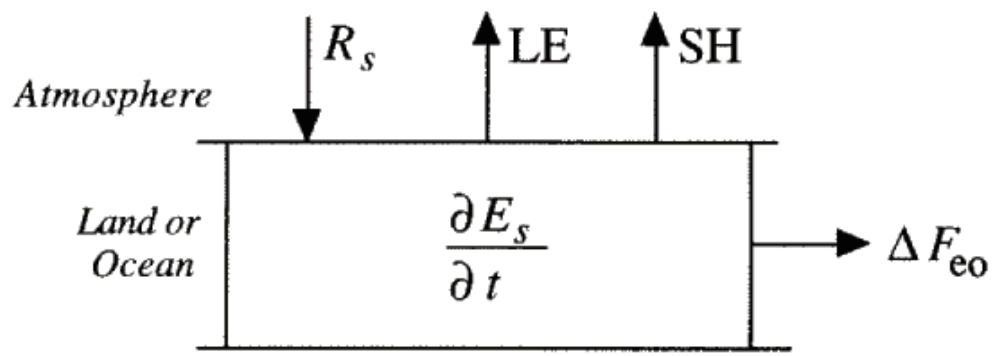

Fig. 4.1 Diagram showing the relationship of the various terms in the surface energy balance (R_s = net radiation, LE = evaporative cooling, SH = sensible cooling, $\partial E_s/\partial t$ = heat storage below the surface, ΔF_{eo} = divergence of horizontal energy flux below the surface).

The albedo of a surface is sensitive to zenith angle…

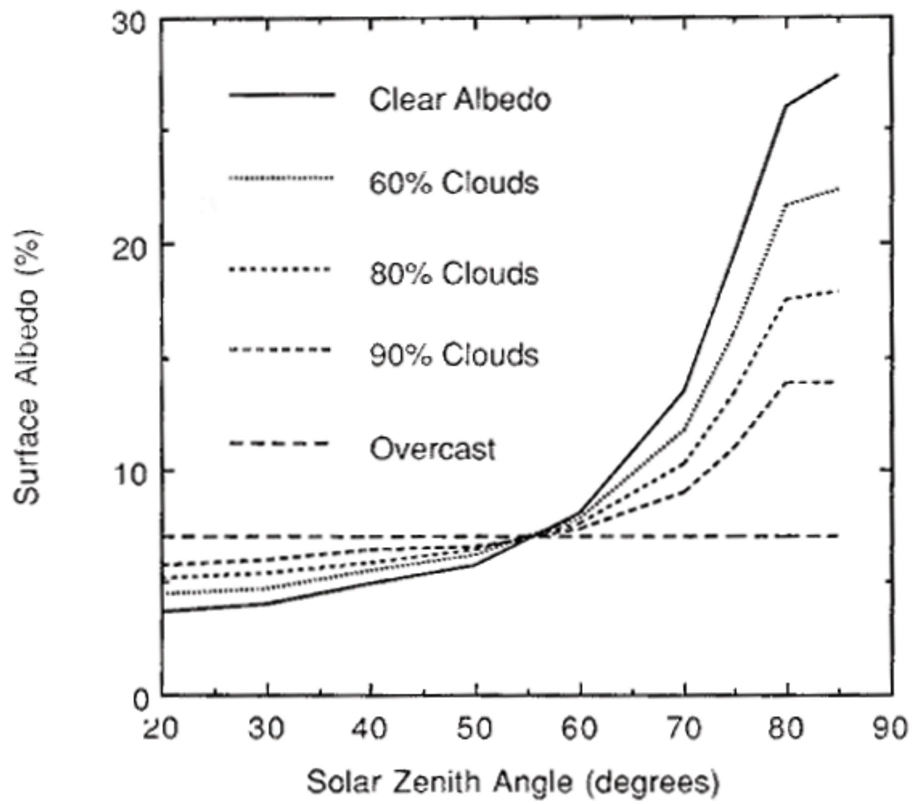

Fig. 4.4 Dependence of the albedo of a water surface on solar zenith angle and cloud cover. [Data from Mirinova (1973).]

The albedo of a surface is sensitive to wavelength…

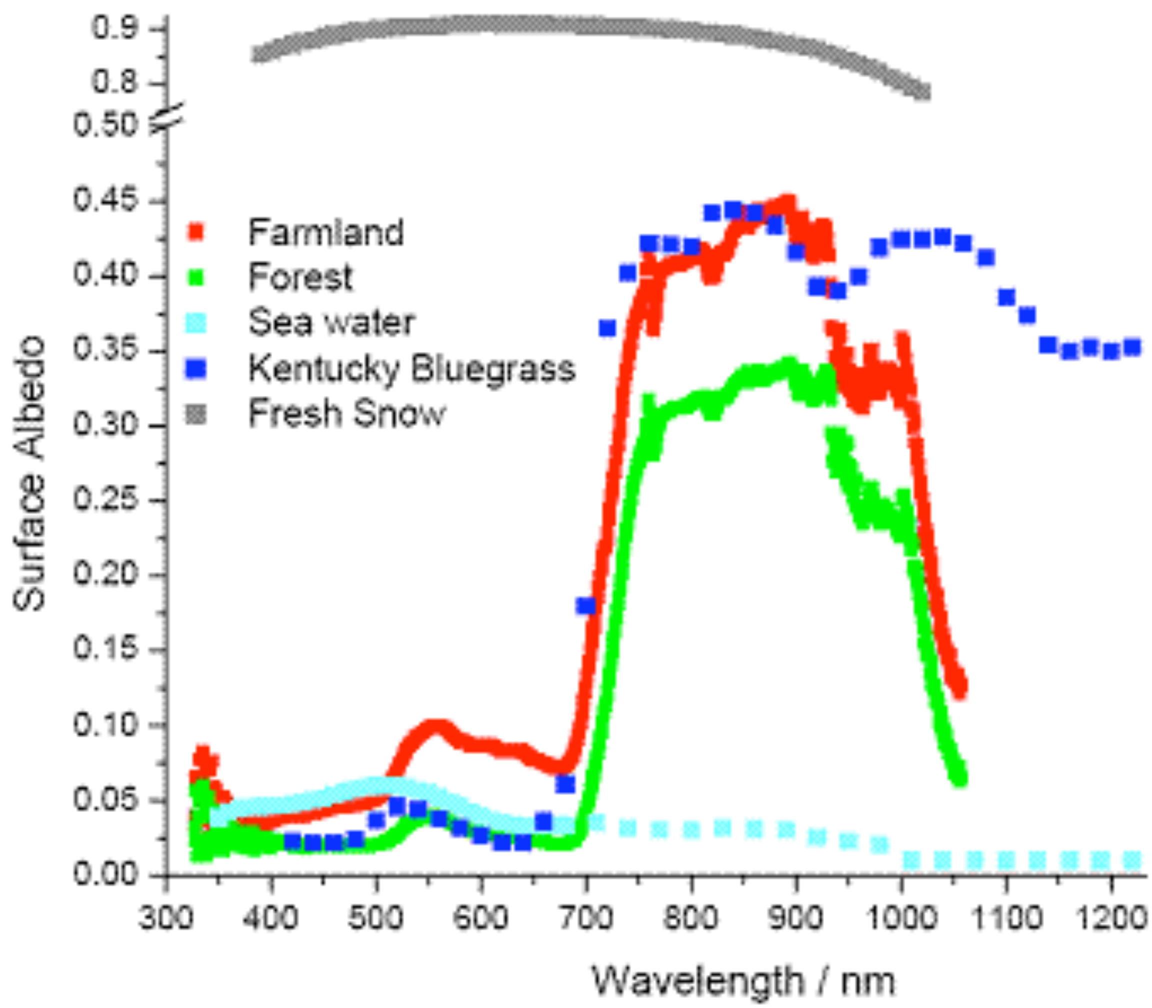

Bowker et al. 1985

Table 4.2

Albedos for Various Surfaces in Percent

Surface type	Range	Typical value
Water		
Deep water: low wind, low altitude	5–10	7
Deep water: high wind, high altitude	10–20	12
Bare surfaces		
Moist dark soil, high humus	5–15	10
Moist gray soil	10–20	15
Dry soil, desert	20–35	30
Wet sand	20–30	25
Dry light sand	30–40	35
Asphalt pavement	5–10	7
Concrete pavement	15–35	20
Vegetation		
Short green vegetation	10–20	17
Dry vegetation	20–30	25
Coniferous forest	10–15	12
Deciduous forest	15–25	17
Snow and ice		
Forest with surface snowcover	20–35	25
Sea ice, no snowcover	25–40	30
Old, melting snow	35–65	50
Dry, cold snow	60–75	70
Fresh, dry snow	70–90	80

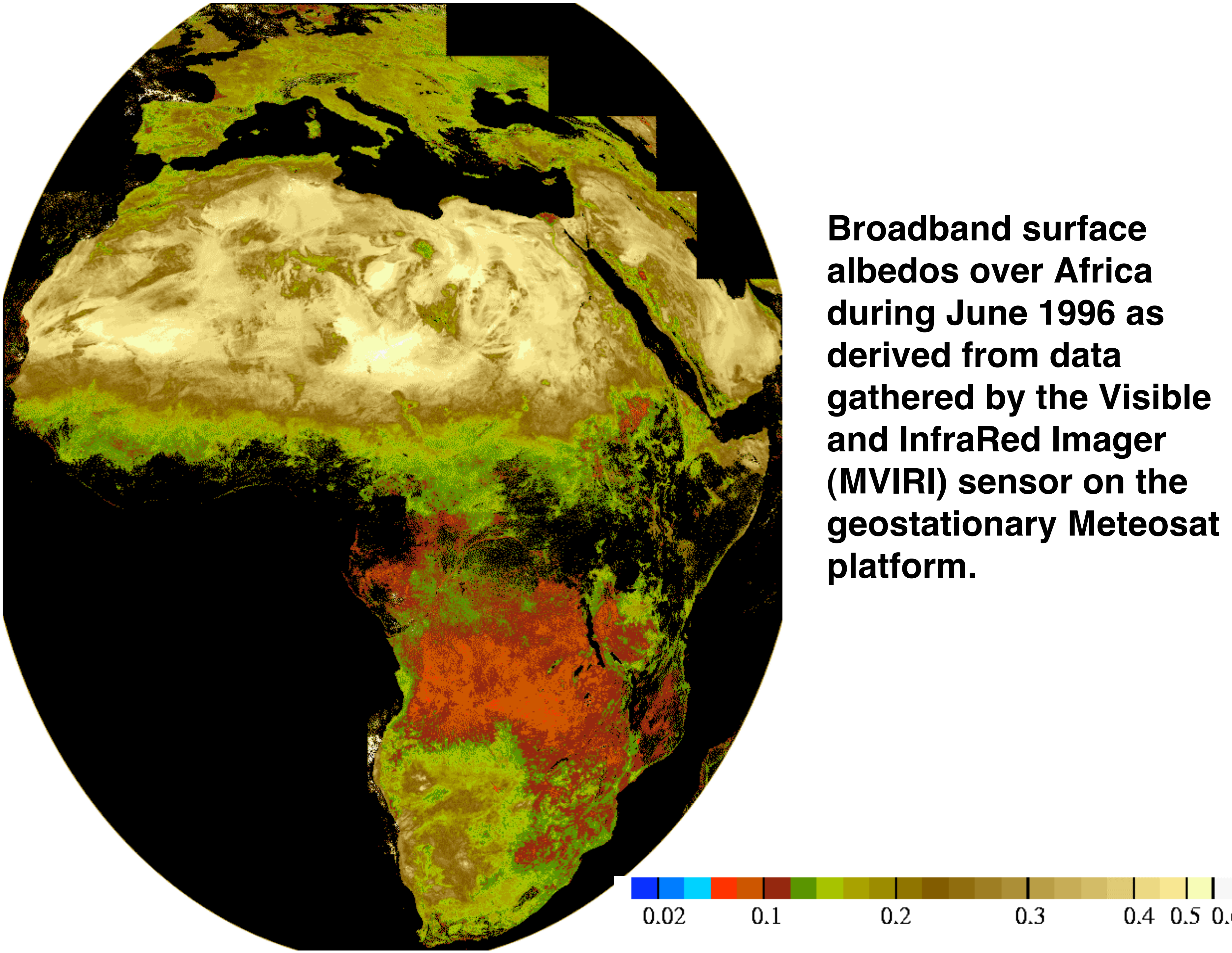

Broadband surface albedos over Africa during June 1996 as derived from data gathered by the Visible and InfraRed Imager (MVIRI) sensor on the geostationary Meteosat platform.

Table 4.4

Infrared Emissivities (percent) of Some Surfaces

Water and soil surfaces		Vegetation	
Water	92–96	Alfalfa, dark green	95
Snow, fresh fallen	82–99.5	Oak leaves	91–95
Snow, ice granules	89	Leaves and plants	
Ice	96	0.8 μm	5–53
Soil, frozen	93–94	1.0 μm	5–60
Sand, dry playa	84	2.4 μm	70–97
Sand, dry light	89–90	10.0 μm	97–98
Sand, wet	95	Miscellaneous	
Gravel, coarse	91–92	Paper, white	89–95
Limestone, light gray	91–92	Glass pane	87–94
Concrete, dry	71–88	Bricks, red	92
Ground, moist, bare	95–98	Plaster, white	91
Ground, dry plowed	90	Wood, planed oak	90
Natural surfaces		Paint, white	91–95
Desert	90–91	Paint, black	88–95
Grass, high dry	90	Paint, aluminum	43–55
Field and shrubs	90	Aluminum foil	1–5
Oak woodland	90	Iron, galvanized	13–28
Pine forest	90	Silver, highly polished	2
		Skin, human	95

[Data from Sellers (1965). Reprinted with permission from the University of Chicago Press.]

The emissivity of most of the earth surfaces is between 0.9 and 1

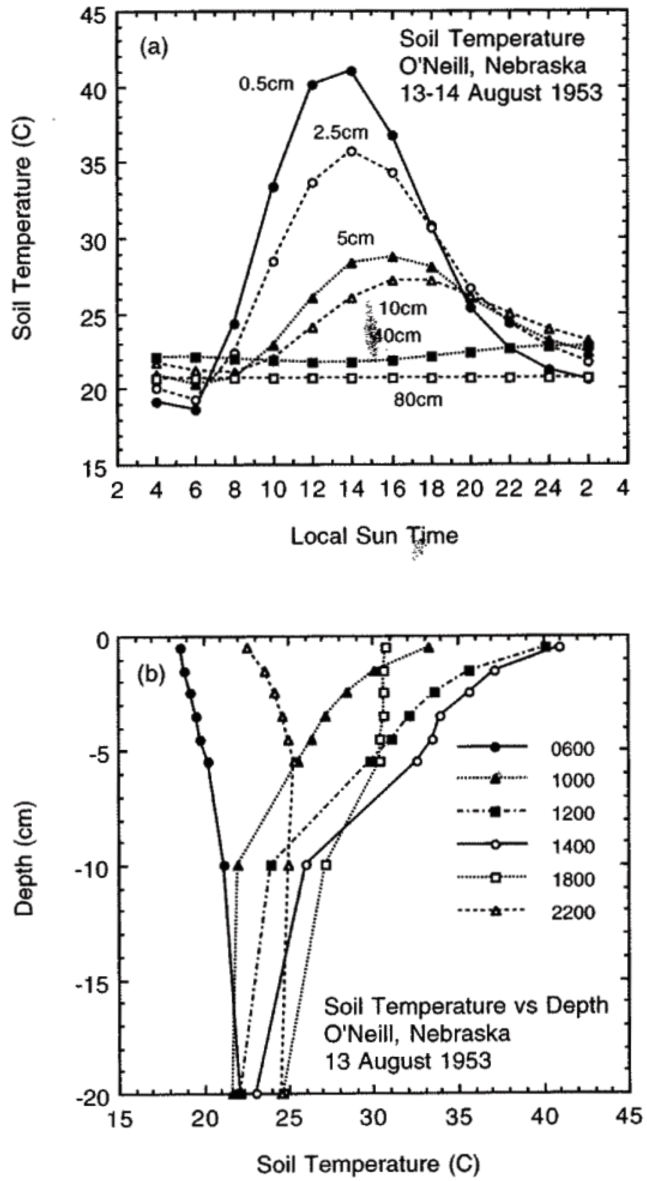

Fig. 4.2 Soil temperature at various depths under a grass field at O'Neill, Nebraska on August 13, 1953: (a) temperature at various depths as a function of local time; (b) temperature as a function of depth at various times. Measured thermal diffusivities on the day illustrated range from 2.5×10^{-7} m^2 s^{-1} at 1 cm to 6×10^{-7} m^2 s^{-1}, at 5-cm depth in the soil. [Data from Lettau and Davidson (1957).]

The effective depth of penetration of temperature anomalies into the soil is determined by the soil's thermal diffusivity and the time scale of the temperature anomaly.

$$h_T = \sqrt{D_T \tau}$$

For the diurnal time scale, the penetration depth is on the order of 10cm.

PLANETARY BOUNDARY LAYER

<u>The hallmark of the *atmospheric boundary layer* is its tight coupling with surface processes.</u>

The depth of the boundary layer, which ranges from tens of meters to a few km, is determined by

(a) the surface heating, which generates *convective turbulence*.

(b) the strength of the winds, and the surface roughness, both of which enhance *mechanical turbulence*.

Diurnal cycle of the boundary layer over land

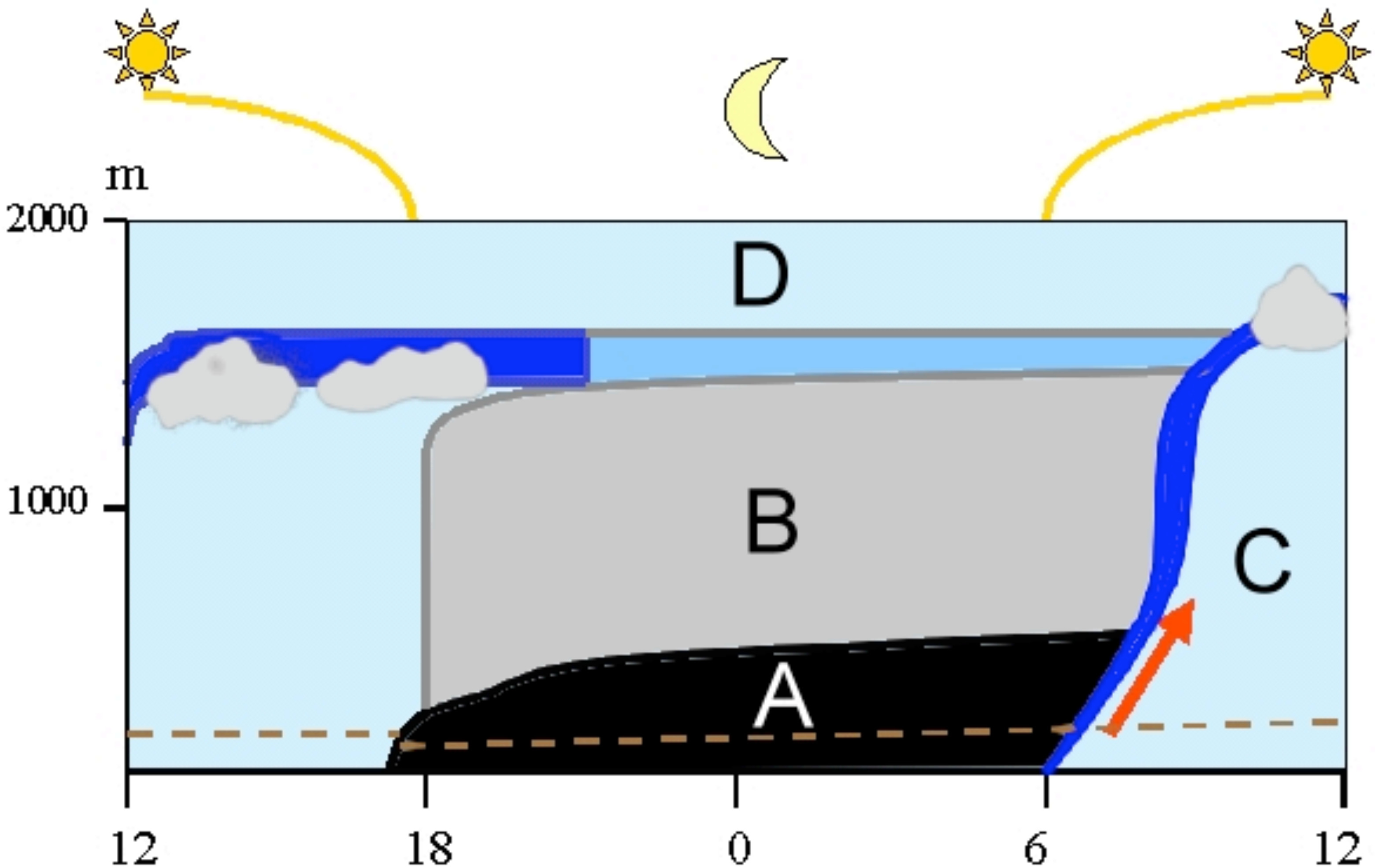

A = stable nocturnal layer

B = residual layer

C = residual layer

D = free troposphere

Diurnal temperature variation in the PBL over land

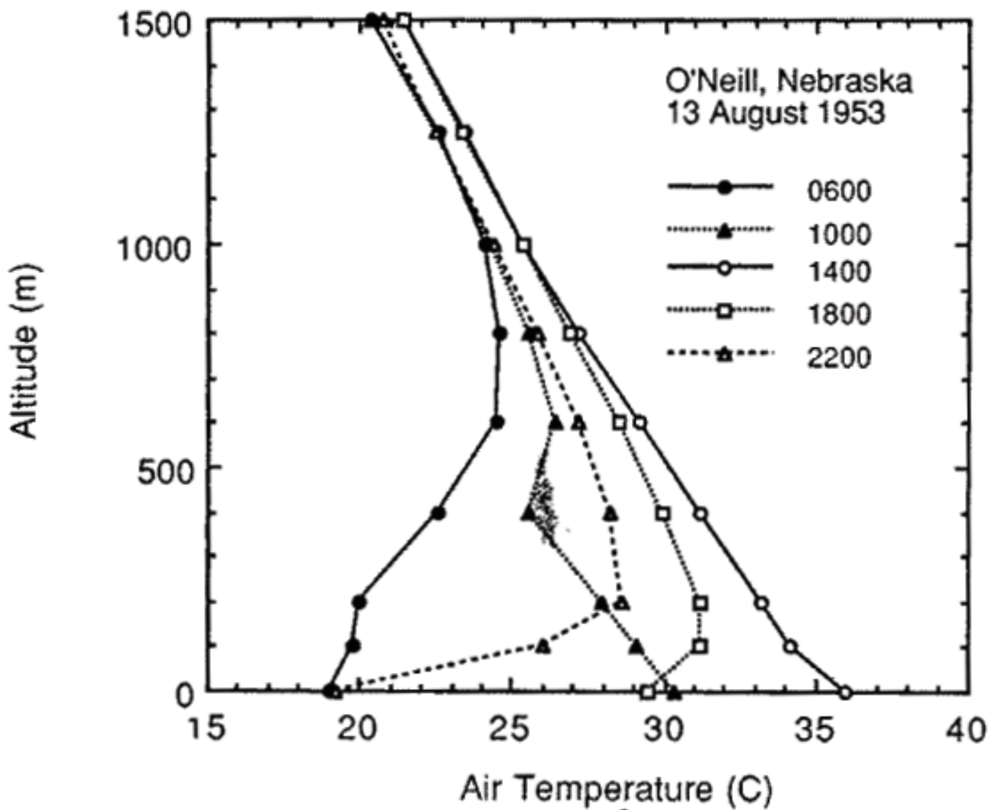

Fig. 4.8 Plot of air temperature at various local times in the lowest 1500 m of the atmosphere at O'Neill, Nebraska on August 13, 1953. Times are given using a 24-hour clock so that 1800 = 6 PM, etc. [Data from Lettau and Davidson (1957).]

Typical vertical profiles of key variables in a boundary layer

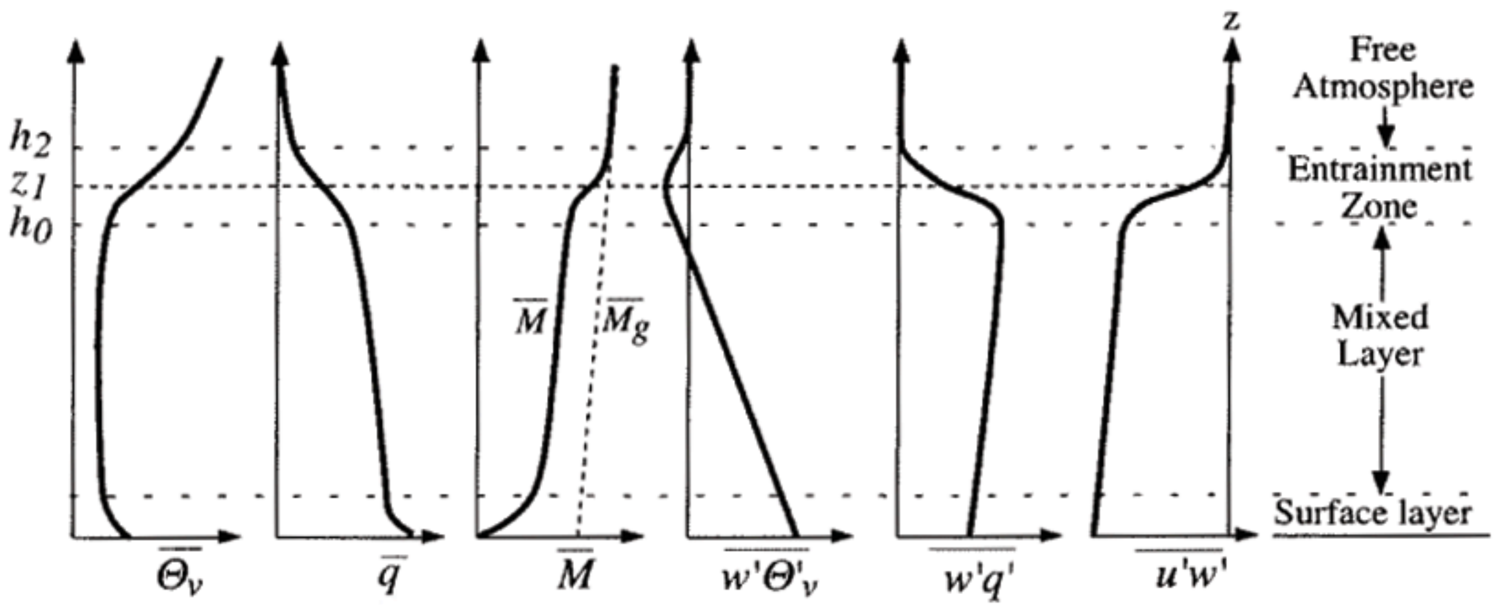

Fig. 4.6 Structure of a convective boundary layer showing the distributions of mean virtual potential temperature $\overline{\Theta}_v$, water vapor mixing ratio $\overline{q}$, momentum $\overline{M}$, geostrophic momentum $\overline{M}_g$, and the vertical eddy fluxes of potential temperature, humidity, and momentum. [From Stull (1988) after Dreidonks and Tennekes (1984). Reprinted with permission from Kluwer Academic Publishers.]

The ***Richardson number*** **is used to characterize the vertical stability of boundary layers.**

$$Ri = \frac{g}{T_o} \frac{\partial\Theta / \partial z}{\left(\partial U / \partial z\right)^2}$$

It is given by the ratio of the vertical potential temperature gradient to the square of the shear. This is a means of comparing the relative importance of convective and mechanical turbulence in deepening the boundary layer.

Tracing the mechanisms of boundary layer turbulence with *Ri*

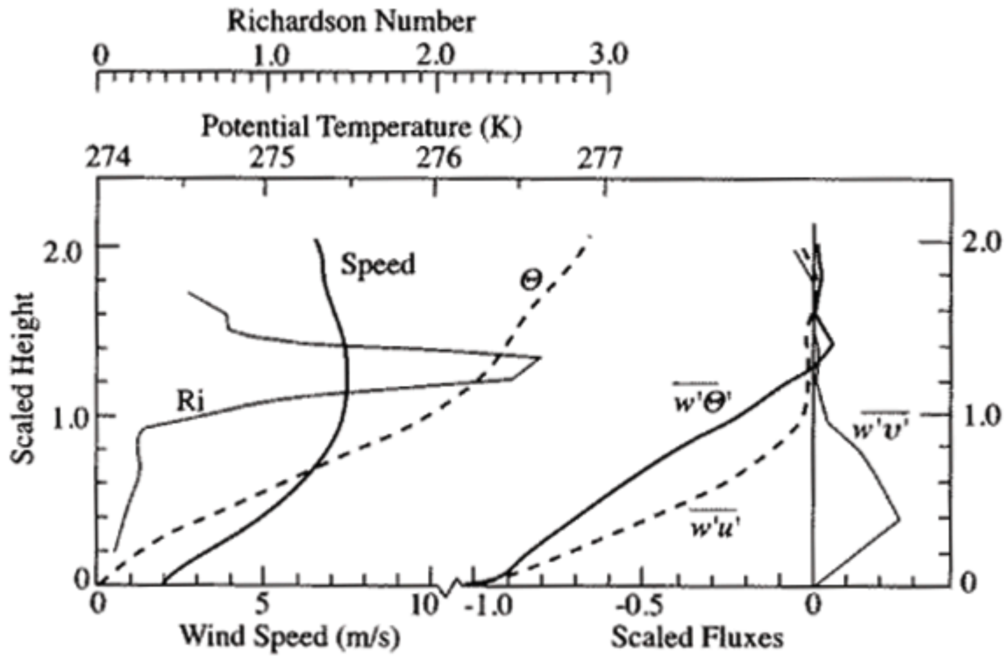

Fig. 4.7 Averaged profiles of wind speed, potential temperature, Richardson number and vertical fluxes of potential temperature $\left(\overline{w'\Theta'}\right)$, and horizontal momentum $\left(\overline{w'u'}\text{ and }\overline{w'v'}\right)$ from nocturnal observations at Haswell, Colorado, on March 24, 1974. The height is scaled by the depth in which turbulence is observed to occur, which on average is about 100 m in this case. Vertical eddy fluxes are scaled by their surface values. [From Mahrt *et al.* (1979). Reprinted with permission from Kluwer Academic Publishers.]

Momentum exchange between the PBL and the free troposphere

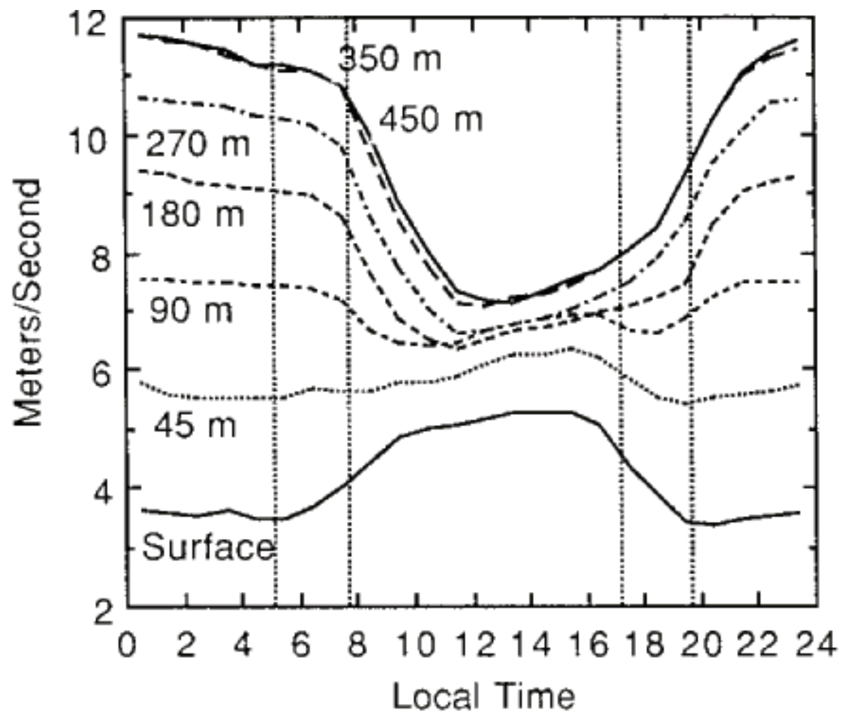

Fig. 4.9 Diurnal cycle of wind speed as a function of height measured from a tower in Oklahoma City and averaged over the period June 1966 to May 1967. [Adapted from Crawford and Hudson (1973). Reprinted with permission from the American Meteorological Society.]

THE DIURNAL CYCLE

Let's begin by considering radiative fluxes only…

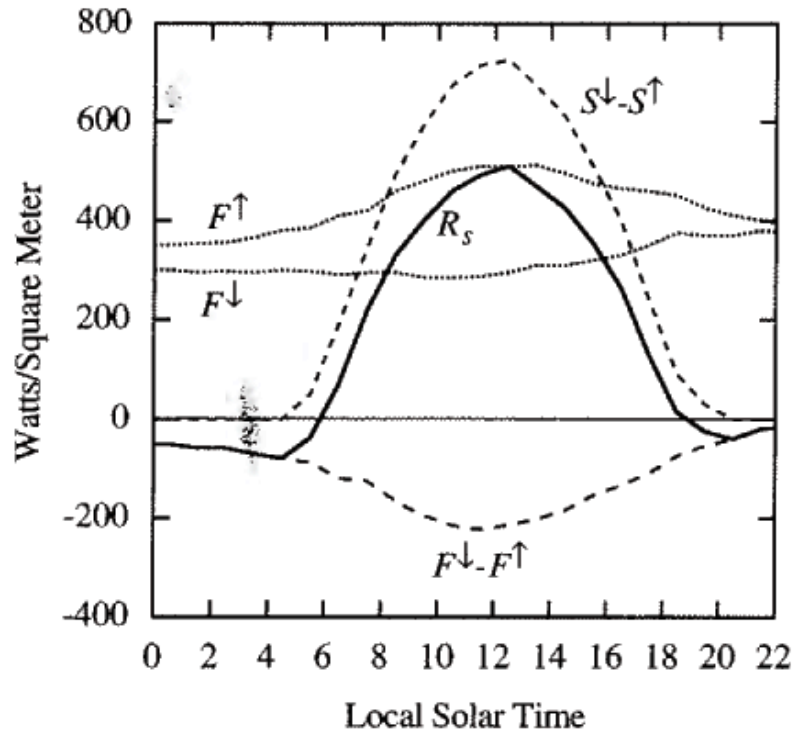

Fig. 4.12 Components of the radiative energy balance for a grass field in Matador, Saskatchewan on July 30, 1971. $F^{\downarrow}$ = downward longwave, $F^{\uparrow}$ = upward longwave, $S^{\downarrow} - S^{\uparrow}$ = net solar, $F^{\downarrow} - F^{\uparrow}$ = net longwave, R_s = net radiation. (After Ripley and Redmann (1976).

Now that we understand what typically controls the behavior of net radiative fluxes, let's examine what balances them, taking the simple case of a desert, where latent heat fluxes are negligible.

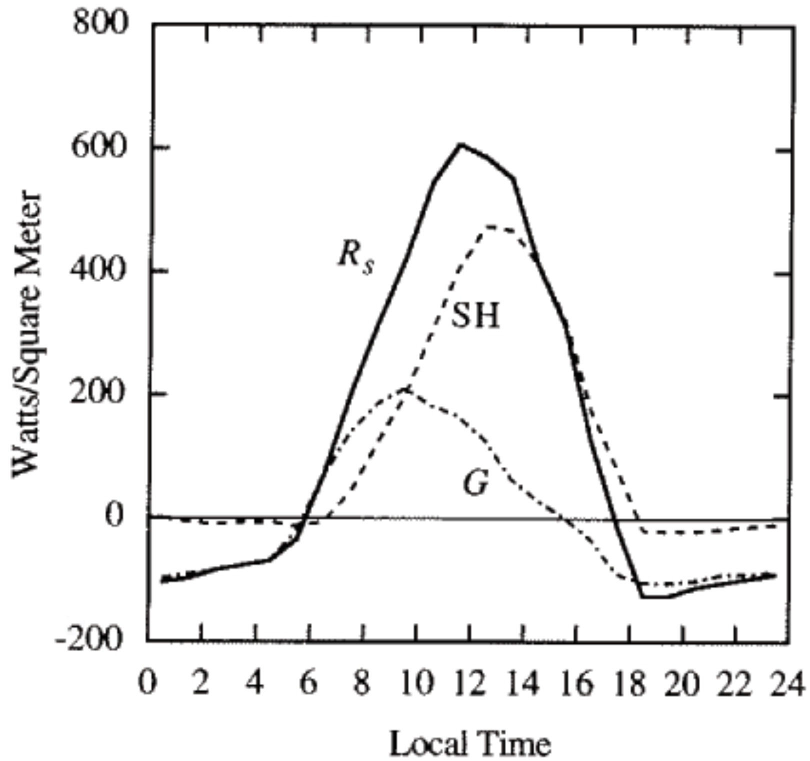

Fig. 4.13 Heat budget for a dry lake bed at El Mirage, California on June 10, 1950. [Data from Vehrencamp (1953). © American Geophysical Union.]

Here's the situation when we add in some moisture…

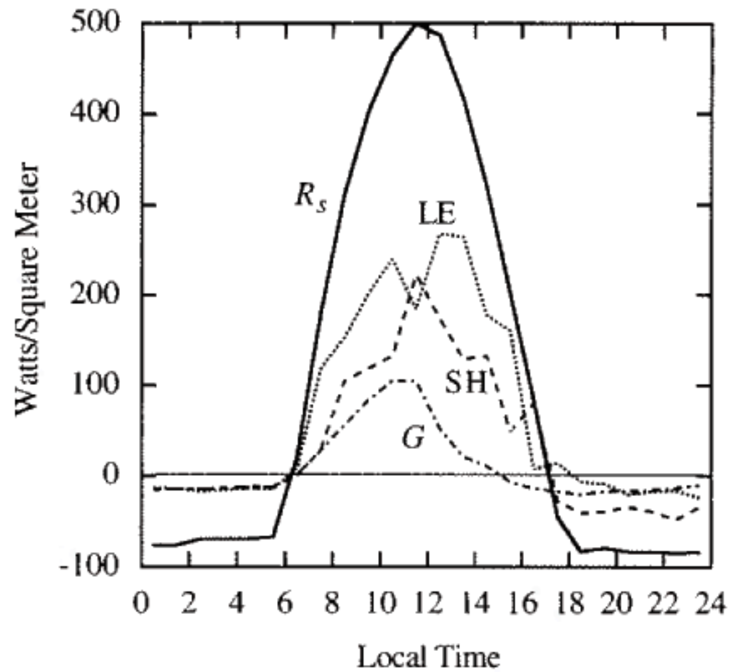

Fig. 4.14 Heat budget for a field of mature corn in Madison, Wisconsin, on September 4, 1952. [Data from Tanner (1960). Reprinted with permission from the Soil Science Society of America.]

And here's the situation when we add a lot of moisture…

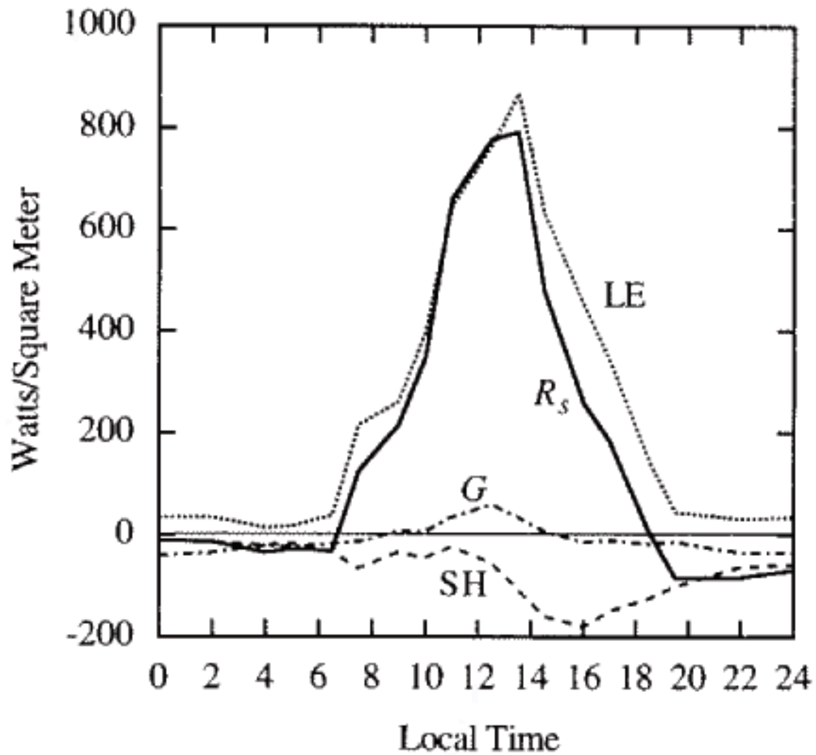

Fig. 4.15 Heat budget for a well-irrigated alfalfa field in Hancock, Wisconsin on July 9, 1956 when the air was advected to the field from a warm dry area. [Data from Tanner (1960). Reprinted with permission from the Soil Science Society of America.]

What would a plot like this look like over the ocean?

THE SEASONAL CYCLE

LAND

The seasonality of the surface heat balance over land is generally governed by a rough balance between net radiation on the one hand, and sensible and latent heating on the other.

What determines the partitioning between sensible and latent heating?

How can you reconcile the nearly negligible storage term with the large seasonal variations in temperature?

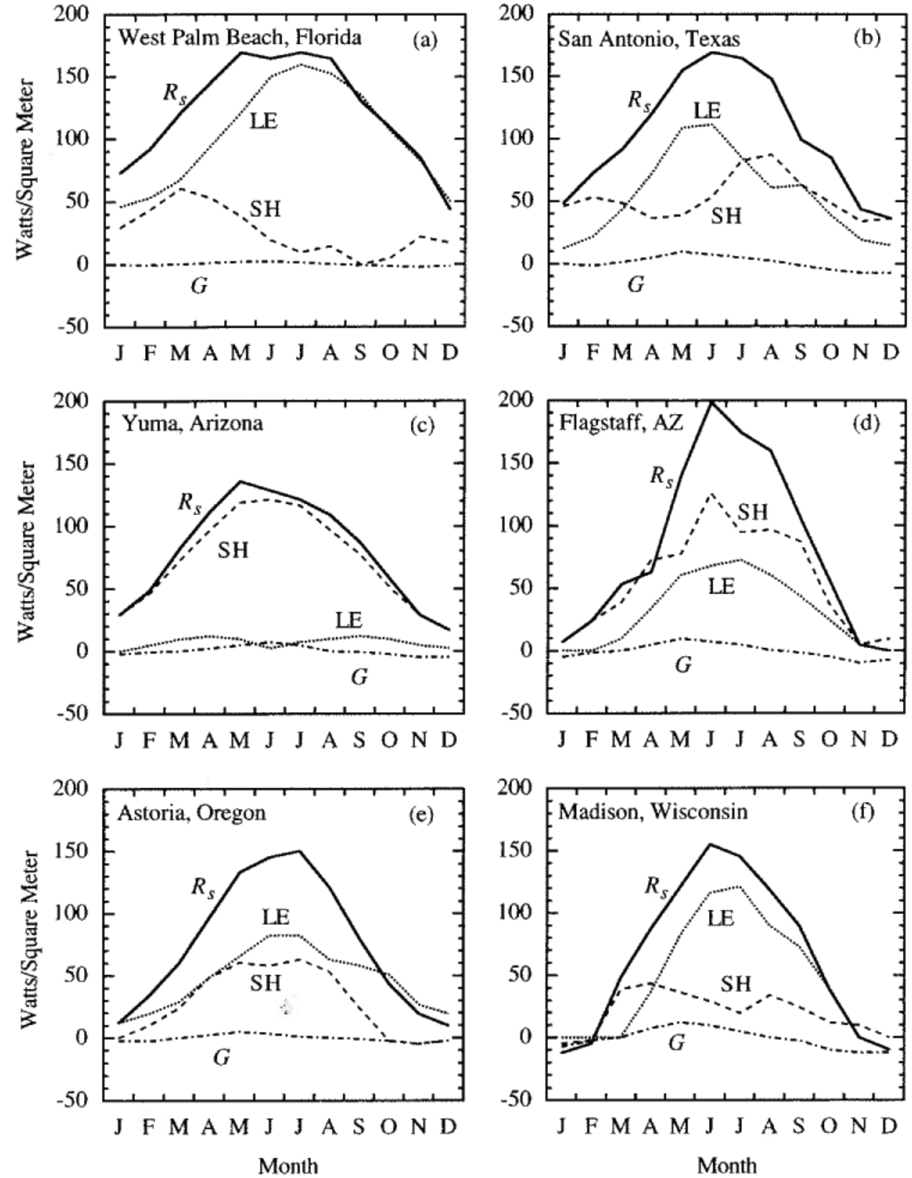

Fig. 4.16 Annual cycle of heat budget components for various midlatitude land locations. [Adapted from Sellers (1965). Reprinted with permission from the University of Chicago Press.]

OCEAN

The large effective heat capacity of the ocean coupled with the effects of currents greatly complicates the seasonal variation of the oceanic surface heat balance.

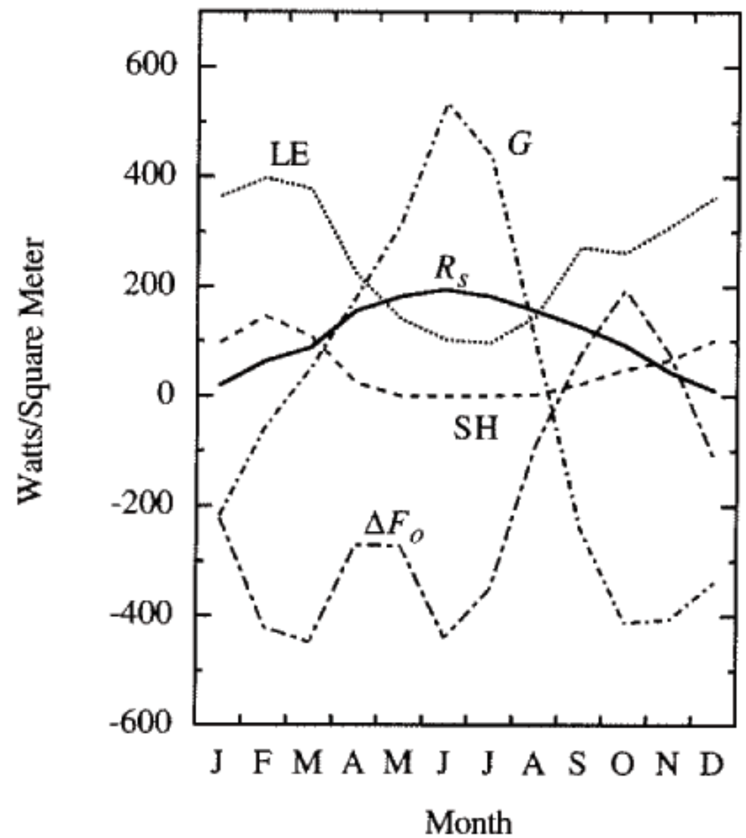

Fig. 4.17 Annual cycle of heat budget components for the Gulf Stream at 38°N, 71°W. (Adapted from Sellers, 1965. Reprinted with permission from the University of Chicago Press.)